A&A 603, A85 (2017)
DOI: 10.1051/0004-6361/201527562

Astronomy & Astrophysics

Search for giant planets in M 67

IV. Survey results⋆,⋆⋆

A. Brucalassi[1,2,3], J. Koppenhoefer[1,2], R. Saglia[1,2], L. Pasquini[3], M. T. Ruiz[4], P. Bonifacio[5], L. R. Bedin[6], M. Libralato[6,7], K. Biazzo[8], C. Melo[9], C. Lovis[10], and S. Randich[11]

[1] Max-Planck für extraterrestrische Physik, 85741 Garching bei München, Germany
[2] University Observatory Munich, Ludwig Maximillian Universitaet, Scheinerstrasse 1, 81679 Munich, Germany
[3] ESO–European Southern Observatory, Karl-Schwarzschild-Strasse 2, 85748 Garching bei München, Germany
e-mail: abrucala@eso.org
[4] Astronomy Department, Universidad de Chile, 1058 Santiago, Chile
[5] GEPI, Observatoire de Paris, PSL Research University, CNRS, place Jules Janssen, 92190 Meudon, France
[6] Istituto Nazionale di Astrofisica, Osservatorio Astronomico di Padova, 35122 Padova, Italy
[7] Università degli Studi di Padova, UNIPD, 35122 Padova, Italy
[8] Istituto Nazionale di Astrofisica, Osservatorio Astrofisico di Catania, 95125 Catania, Italy
[9] ESO–European Southern Observatory, 3107 Santiago, Chile
[10] Observatoire de Genève, Sauverny, 1290 Versoix, Switzerland
[11] Istituto Nazionale di Astrofisica, Osservatorio Astrofisico di Arcetri, 50125 Firenze, Italy

Received 15 November 2015 / Accepted 26 February 2017

ABSTRACT

Context. We present the results of a seven-year-long radial velocity survey of a sample of 88 main-sequence and evolved stars to reveal signatures of Jupiter-mass planets in the solar-age and solar-metallicity open cluster M 67.
Aims. We aim at studying the frequency of giant planets in this cluster with respect to the field stars. In addition, our sample is also ideal to perform a long-term study to compare the chemical composition of stars with and without giant planets in detail.
Methods. We analyzed precise radial velocity (RV) measurements obtained with the HARPS spectrograph at the European Southern Observatory (La Silla), the SOPHIE spectrograph at the Observatoire de Haute-Provence (France), the HRS spectrograph at the Hobby Eberly Telescope (Texas), and the HARPS-N spectrograph at the Telescopio Nazionale *Galileo* (La Palma). Additional RV data come from the CORALIE spectrograph at the *Euler* Swiss Telescope (La Silla). We conducted Monte Carlo simulations to estimate the occurrence rate of giant planets in our radial velocity survey. We considered orbital periods between 1.0 day and 1000 days and planet masses between 0.2 M_J and 10.0 M_J. We used a measure of the observational detection efficiency to determine the frequency of planets for each star.
Results. All the planets previously announced in this RV campaign with their properties are summarized here: 3 hot Jupiters around the main-sequence stars YBP1194, YBP1514, and YBP401, and 1 giant planet around the evolved star S364. Two additional planet candidates around the stars YBP778 and S978 are also analyzed in the present work. We discuss stars that exhibit large RV variability or trends individually. For 2 additional stars, long-term trends are compatible with new binary candidates or substellar objects, which increases the total number of binary candidates detected in our campaign to 14. Based on the Doppler-detected planets discovered in this survey, we find an occurrence of giant planets of $\sim 18.0^{+12.0}_{-8.0}$% in the selected period-mass range. This frequency is slightly higher but consistent within the errors with the estimate for the field stars, which leads to the general conclusion that open cluster and field statistics agree. However, we find that the rate of hot Jupiters in the cluster ($\sim 5.7^{+5.5}_{-3.0}$%) is substantially higher than in the field.

Key words. techniques: radial velocities – planets and satellites: gaseous planets

1. Introduction

In recent years, several observational campaigns have been dedicated to search for planets in clusters or stellar associations, where the majority of stars is considered to form. Stars in clusters constitute a homogeneous sample in age and chemical composition that is ideal for investigating the dependence of planet formation on the mass and the properties of the central star (González Hernández et al. 2013, 2010; Baumann et al. 2010; Johnson et al. 2010; Ramírez et al. 2010; Meléndez et al. 2009), for determining the formation timescale and distinguishing different migration processes (Dong et al. 2014; Quinn et al. 2014; Dawson & Murray-Clay 2013), and finally for modeling the effects of stellar encounters on the formation and evolution of planetary systems (Li & Adams 2015; Cai et al. 2016; Shara et al. 2016; Davies et al. 2014; Malmberg et al. 2011; Spurzem et al. 2009). However, the high-precision radial velocity (RV) technique and the transit method have been successful

⋆ Based on observations collected at the ESO 3.6m telescope (La Silla), at the 1.93 m telescope of the Observatoire de Haute-Provence (OHP, France), at the Hobby Eberly Telescope (HET, Texas), at the Telescopio Nazionale *Galileo* (TNG, La Palma) and at the Euler Swiss Telescope (La Silla).
⋆⋆ Individual RV measurements are available at the CDS via anonymous ftp to cdsarc.u-strasbg.fr (130.79.128.5) or via http://cdsarc.u-strasbg.fr/viz-bin/qcat?J/A+A/603/A85

only very recently in discovering planetary-mass companions around stars belonging to open clusters (OC). Of the most recent results in this field, we mention the detection of a hot Jupiter and a multi-planetary system in the Praesepe OC (Quinn et al. 2012; Malavolta et al. 2016), of a hot Jupiter in the Hyades (Quinn et al. 2014), of two sub-Neptune planets in NGC 6811 (Meibom et al. 2013), and the discovery of five Jupiter-mass planets in M 67 (Brucalassi et al. 2014, 2016). Previous RV surveys provided detections of a long-period giant planet around one of the Hyades clump giants (Sato et al. 2007) and a substellar-mass object in NGC 2423 (Lovis & Mayor 2007). No significant exoplanet candidates have been found by either ground- or by space-based transit campaigns in globular clusters (Gilliland et al. 2000; Nascimbeni et al. 2012).

These discoveries confirm that giant planets exist in a dense cluster environment, and suggest that a complete census of planet discoveries may be biased by the detection limit of the instruments and the observations available today. Moreover, results from various simulations show that dense birth environments such as stellar clusters can significantly influence the planet formation process and the resulting orbital properties of the planetary systems. Close encounters between stars or binary companions can modify the structure of any planetary system and also subsequently generate strong interactions between planets over very long timescales (Davies et al. 2014; Malmberg et al. 2011). This leads to the ejection of some planets, but it also seems to favor the conditions for the formation of hot Jupiters (Shara et al. 2016). Studying hot Jupiters in OCs can therefore shed light onto the long-standing problem of identifying their dynamical origin.

For the past seven years we have carried out a search for massive planets around main-sequence (MS) and evolved stars in the OC M 67. The scientific motivations for these studies include determining the impact of a different environment on the frequency and the evolution of planetary systems with respect to field stars. As a long-term goal, we aim to study the connection between giant planet formation and stellar mass and chemical composition. M 67 is the perfect target to search for planets around OC stars. Chemical analysis from several works (Randich et al. 2006; Pace et al. 2008; Önehag et al. 2011, 2014) has shown that M 67 has a chemical composition (not only Fe, but also the other elements) that is extremely similar to solar, as close as allowed by the precision of the measurements. In addition, the age of M 67 (3–5 Gyr), according to numerous determinations, encompasses the accepted value of the Sun, while the age determination for field stars is always rather uncertain. Finally, M 67 is a rich OC, which gives us the opportunity to find many stellar candidates that share similar properties and a large number of stars with different masses, characteristics that are essential to address the questions above.

Through RV measurements obtained with HARPS at La Silla-ESO, SOPHIE at OHP, HRS at HET, HARPS-N at the TNG, and CORALIE at the *Euler* Swiss Telescope, five new giant planets have been discovered around M 67 stars (Brucalassi et al. 2014, 2016): three hot Jupiters around MS stars, and two long-period planets around evolved stars.

In this paper, we present our RV campaign around stars of the OC M 67 considering data obtained until March 2015, and we provide a complete census of all the stars.

The star sample is described in Sect. 2, RV observations and analyses are reported in Sect. 3. In Sect. 4 we provide more detailed information on individual objects. In Sect. 5 we report a series of simulations based on a Monte Carlo approach that we used to estimate the occurrence rate of giant planets in our radial velocity survey. Finally, we summarize our results in Sect. 6.

Table 1. List of the observations.

Instrument	H	S	HET	C	HN
N. Stars	88	70	24	14	13
Observations	734	168	125	99	23
MS	481	75	59	0	12
TO	63	22	23	0	7
G	190	78	43	99	4

Notes. The table lists: number of observed stars, total number of observations, number of main-sequence (MS), turn-off (TO), and giant (G) stars observed for each instrument. HARPS (H), SOPHIE (S), HET, CORALIE (C), and HARPS-N (HN).

2. Sample and observations

A complete description of the sample is reported in our previous works (Pasquini et al. 2012; Brucalassi et al. 2014). We highlight here those characteristics that are most relevant for the aim of this paper.

The original M 67 sample includes a total of 88 stars with V mag between 9 and 15, and a mass range of 0.9–1.4 $M_{\odot}$.

Main-sequence stars have been selected following Pasquini et al. (2008). In particular, we considered those stars with a membership probability higher than 60% and a proper motion lower than 6 mas/yr with respect to the average according to Yadav et al. (2008). When we considered the selection of the giants, we referred to Sanders (1977) for the membership probability, and the RV membership was derived according to Mermilliod & Mayor (2007) and Mathieu et al. (1986). We are aware that several stars that are particularly close to the turn-off point, although fulfilling our selection criteria, have been not observed because the observation time was too short.

Five different telescopes and instrument combinations have been used to obtain the RV measurements. Table 1 summarizes the number of the observations for each instrument.

The HARPS spectrograph (Mayor et al. 2003) at the ESO 3.6 m telescope was used in high-efficiency mode (EGGS mode) since the M 67 stars are quite faint for this instrument. In this configuration the fiber has an aperture on the sky of 1.2 arcsec, corresponding to $R = 90\,000$, and is not equipped with an optical scrambler. The precision is limited to 5–7 $\mathrm{m\,s^{-1}}$, but the efficiency is 30–40% better than the high-resolution mode (HAM mode), which allows us to obtain the highest resolving power of 115 000 with a fiber aperture of 1 arcsec. The spectral range covered is 378–691 nm. Exposure times ranged from 10 to 45 min, yielding a typical signal-to-noise ratio (S/N) per resolution element of 10 to 15 for the faintest stars. Between January 2008 and March 2015, we gathered 734 observations of 88 stars with HARPS with an associated internal precision of $\sim$10 $\mathrm{m\,s^{-1}}$. These observations represent the majority of this survey, and we therefore consider HARPS as our reference.

The SOPHIE spectrograph (Bouchy & Sophie Team 2006) at the OHP 1.93 m telescope was used in high-efficiency mode with $R = 40\,000$ and a spectral range of 387–694 nm. We analyzed 168 SOPHIE observations of 70 M 67 stars with an associated internal precision of $\sim$12 $\mathrm{m\,s^{-1}}$.

For the HRS spectrograph (Tull et al. 1998) at the Hobby Eberly Telescope we opted for a configuration with $R = 60\,000$

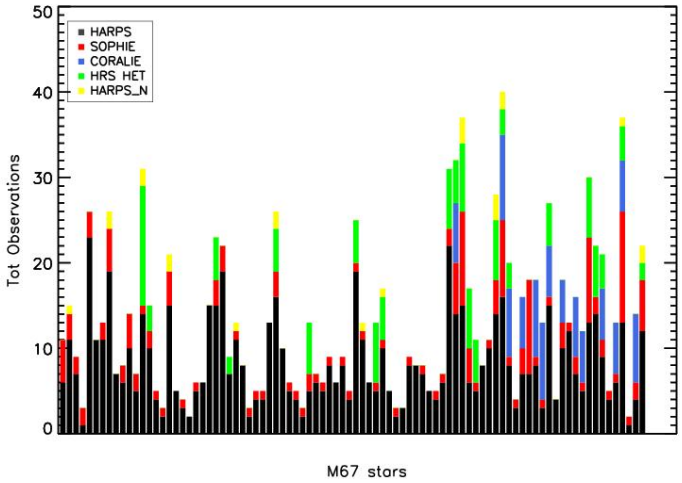

Fig. 1. Histogram showing the number of observations per star for our total sample. All observations from HARPS, HARPS-N, SOPHIE, CORALIE, and HET HRS are included in the plot and updated to March 31, 2015. The order number of the stars corresponds to Table A.1.

and a wavelength range of 407.6–787.5 nm. We obtained 125 observations for 24 stars with a typical error bar associated with the observations of ~25 m s^{-1}. During the period 2013–2015, the HET telescope was not accessible because of a telescope upgrade.

Moreover, we gathered 99 RV data points for 14 giant stars observed between 2003 and 2005 (Lovis & Mayor 2007) with the CORALIE spectrograph at the 1.2 m *Euler* Swiss telescope.

In addition, 27 h in service mode have been allocated with the TNG on La Palma Canary Island and the HARPS-N spectrograph. The HARPS-N is a fiber-fed echelle spectrograph, similar to HARPS on the 3.6 m ESO telescope and covers the wavelength range between 383 to 693 nm, with a spectral resolution R = 115 000. The two HARPS fibers (object + Sky/ThAr) have an aperture on the sky of 1 arcsec and are equipped with an image scrambler to provide a uniform spectrograph pupil illumination. Unfortunately, the observing campaign during the winter 2013–2014 was not very successful. The run at the TNG was impacted by bad weather and only 10 observing hours could be used, with 23 spectra for 13 stars.

Figure 1 shows a histogram with the number of observations per star updated to March 31, 2015. We have obtained 13 observations per star on average: 10 observations per star for MS stars, and 18 observations per star for giants and turn-off stars. Table A.1 shows the main data for the observed stars. In addition to the basic stellar parameters, the number of observations per star is given for each spectrograph and as a total.

3. RV analysis

HARPS, SOPHIE, and HARPS-N are provided with a similar automatic pipeline. The spectra are extracted from the detector images and cross-correlated with a numerical mask. For all of our stars, irrespective of the spectral type and luminosity, we used a G2V mask obtained from Sun spectra. Radial velocities are derived by fitting each resulting cross-correlation function (CCF) with a Gaussian (Baranne et al. 1996; Pepe et al. 2002). This real-time pipeline also provides an associated internal RV error $\sigma_{\rm pn}$ (photon noise error).

For the HRS data, the radial velocities were computed using a series of dedicated routines based on IRAF[1]. The procedures are described in more detail in Cappetta et al. (2012). The different steps include the wavelength calibration using a Th-Ar lamp exposure acquired before and after each stellar spectrum, the normalization of the spectra, the cleaning of cosmic rays as well as telluric and sky lines, the cross-correlation of the spectrum performed order by order with a G2V star template, and finally, the computation of the heliocentric corrections. The resulting CCFs were fitted with a Gaussian function to determine the RVs. After the orders affected by telluric lines and low S/N are rejected, the final RV value is given by the average value over the retained orders. Finally, the internal RV uncertainties are calculated by $\sigma_{\rm pn} = {\rm rms}(v)/\sqrt{N}$, where v is the RV of the individual orders and N is the number of the orders.

We used nightly observations of the RV standard star HD32923 to correct all observations for each star to the zero-point of HARPS (as explained in Pasquini et al. 2012) and to take any instrument instability or any systematic velocity shifts between runs (such as the modification of the SOPHIE fiber link in June 2011 (Perruchot et al. 2011) or technical problems during the calibration phase at HARPS) into account. An additional correction was applied to the SOPHIE data to account for the low S/N of the observations. For this, we corrected our spectra using Eq. (1) in Santerne et al. (2012). Finally, we considered the total error of the RV measurements ($\sigma_{\rm obs}$) to be the sum in quadrature of all RV error sources described above. After all the observations for each star were corrected to the zero-point of HARPS, they were analyzed together. The combined measurement uncertainties have been compared to the observed velocity dispersions to evaluate the significance of any potential velocity variation and to highlight any possible outliers that would suggest the presence of exoplanets. In Table A.1 the mean stellar RV of each star is given, together with the average associated error ($\sigma_{\rm obs}$) and the RV dispersion of the observations ($\sigma_{\rm RV}$). Figure 2 shows (top panel) the histogram of the observed RV scatter ($\sigma_{\rm RV}$) for the sample stars. Binary candidates were excluded, and the stars with significant RV trend are not shown. The bulk of our observations have an RV scatter represented by a Gaussian distribution centered on ~21 ± 7 m s^{-1}. Stars with an RV variability at or above 40 m s^{-1} are considered very good candidates for low-mass companion hosts.

Figure 2 also includes a second panel (bottom) showing the histogram of the ratio between the observed RV scatter ($\sigma_{\rm RV}$) and the average associated error ($\sigma_{\rm obs}$) for each star. Large variations for planet candidates or long-term objects (see Sect. 4) are easy to identify. A clear peak results for most of the stars. Considering only stars with $\sigma_{\rm RV} < 4\sigma_{\rm obs}$ (the small variations) and with no suspected companions, we calculated a peak of ~1.3 (employing a kernel density estimator to smooth the distribution), which is a sign that we may have underestimated the measurement errors. However, halos of excess scatter (RV variability) are present, which are most likely due to a combination of effects. In evolved stars some measurable intrinsic RV variability is present, as shown also in Setiawan et al. (2004) and Hekker et al. (2008), while for the faint MS stars the uncertainty in the measurements increases because of the limited S/N. Finally, some of the stars still have only a few observational points with poorly constrained RV variability, and their scatter is very likely the result of our low data statistics. Pasquini et al. (2012) also investigated whether other instrumental effects such as the observed flux or airmass (not included in the data analysis) could

[1] http://iraf.noao.edu/

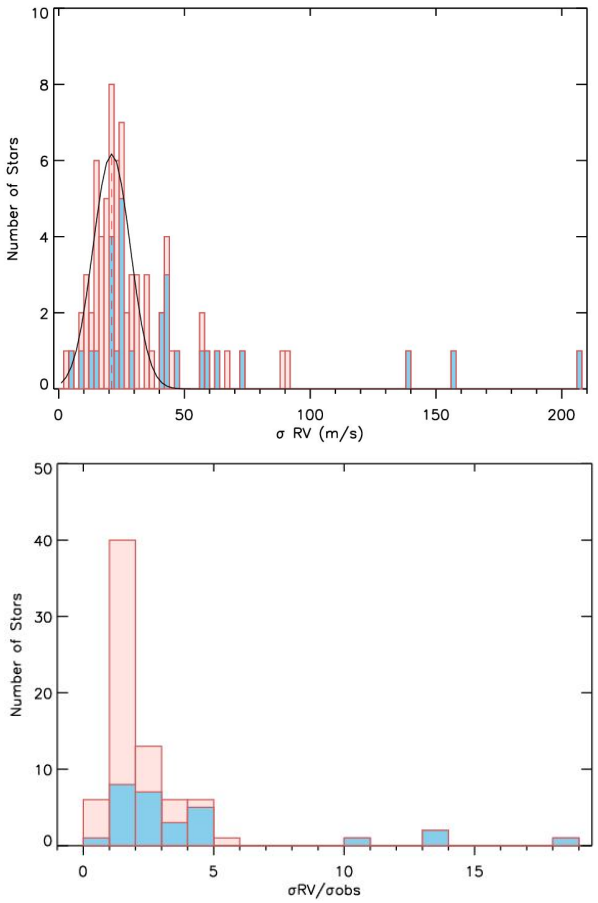

Fig. 2. *Top*: histogram showing the observed velocity dispersions (σ_{RV}) for the MS stars (pink) and giants and turn-off stars (blue) of our sample. Binary candidates and stars with high RV trend have been excluded. The black line represents the Gaussian fit centered at ~21 m s^{-1} of width $\sigma \sim 7$ m s^{-1}. *Bottom*: histogram showing the ratio of the RV dispersion (σ_{RV}) and the average measurements error (σ_{obs}). The symbols are the same as in *the top panel*.

affect the RV measurement precision at low count levels, but no correlation was found. In order to consider these effects during the computation of the giant planet occurrence rate (see Sect. 5), we empirically inflated the estimated errors by adding in quadrature a term (σ'_{RV}) equivalent, on average, to the excess RV scatter. This is calculated by $\sigma'_{RV} = \sqrt{\bar{\sigma}^2_{RV,st} - \bar{\sigma}^2_{obs,st}}$, where $\bar{\sigma}^2_{RV,st}$ and $\bar{\sigma}^2_{obs,st}$ are the mean RV scatter and the mean estimated error, respectively, of stars without a trend and suspected companions. In Table A.1 the corrected associated error for each star is reported as σ_{cor}.

We studied the RV variations of our target stars by computing the Lomb-Scargle periodogram (Scargle 1982; Horne & Baliunas 1986). This is a commonly used technique for searching for periodic sinusoidal signals in unevenly sampled data and allows estimates of the detection threshold to be written down for periods shorter than the duration of the observations (Horne & Baliunas 1986). The significance of the sinusoid best fit of our RV values was determined by analytically calculating the false-alarm probability (FAP) level (Horne & Baliunas 1986). Afterward, we applied Levenberg-Marquardt analysis (Wright & Howard 2009, RVLIN) to fit Keplerian orbits to the radial velocity data.

Table 2. RV measurements, RV uncertainties, and instrument.

Star	BJD (–2 450 000)	RV (km s^{-1})	σ_{obs} (km s^{-1})	Instrument
YBP266	4488.509042	33.78637	0.012	SOPHIE
	4855.591058	33.77123	0.012	HARPS
	4859.605234	33.77318	0.014	HARPS
	4862.702784	33.77678	0.017	HARPS
	5189.693914	33.79851	0.017	HARPS

Notes. All RV data points are corrected to the zero-point of HARPS. The errors σ_{obs} do not include the correction for the excess RV scatter (see Sect. 3).

Radial velocity periodic variation can be caused by rotational inhomogeneities related to stellar surface activity, such as plages or spots, including the one that is due to magnetic cycles of several years (Santos et al. 2010). Stellar activity can be diagnosed with spectral indicators or by monitoring the shape of the spectral lines. The low S/N of our observations does not provide sufficient signal in the region of the sensitive Ca II H and K lines. We therefore followed a method similar to the one described in Pasquini & Pallavicini (1991). We investigated the presence and variability of chromospheric active regions in these stars by measuring the variations of the core of Hα with respect to the continuum (see Dollinger 2008, for a more detailed description of how the Hα was measured). For each case we verified the correlation between the RVs and the bisector span of the CCF (calculated following Queloz et al. 2001) or with the FWHM of the CCF.

4. Results

In the following, we describe the general results of our survey and discuss our analyses and interpretation of the RV time series for the most relevant targets in more detail. In particular, two further planet candidates are reported in this work. For the other stars, we refer to Table A.1, in which the main data for the observed objects are summarized. Individual RV measurements for all the stars are provided at the CDS in the format listed in Table 2.

4.1. Binary candidates

Twelve binary candidates were previously published in Pasquini et al. (2012). Here we present two other MS stars in the sample (YBP1051, YBP673) that either show significant linear trends or RV variations that are too large to be produced by an exoplanet or by a non-stellar object. The RV measurements of these stars are shown in Fig. 3. They display a peak-to-peak RV amplitude of ~1.0 km s^{-1} with an RV range spanned over more than six years. All binaries are highlighted in boldface in Table A.1.

4.2. Planets and planetary candidates

Four planets were announced in our previous works (Brucalassi et al. 2014, 2016) for the stars YBP401, YBP1194, YBP1514, and S364. Table 3 reports the main stellar characteristics and the resulting updated orbital parameters of the Keplerian fit for all these stars. Another two stars (S978 and YBP778) show significant indication for the presence of Jovian-mass companions.

YBP778. Twenty-one RV measurements have been obtained for the MS star YBP778 since 2009: 15 with HARPS, the others with SOPHIE and HARPS-N. The typical S/N is 10 and the

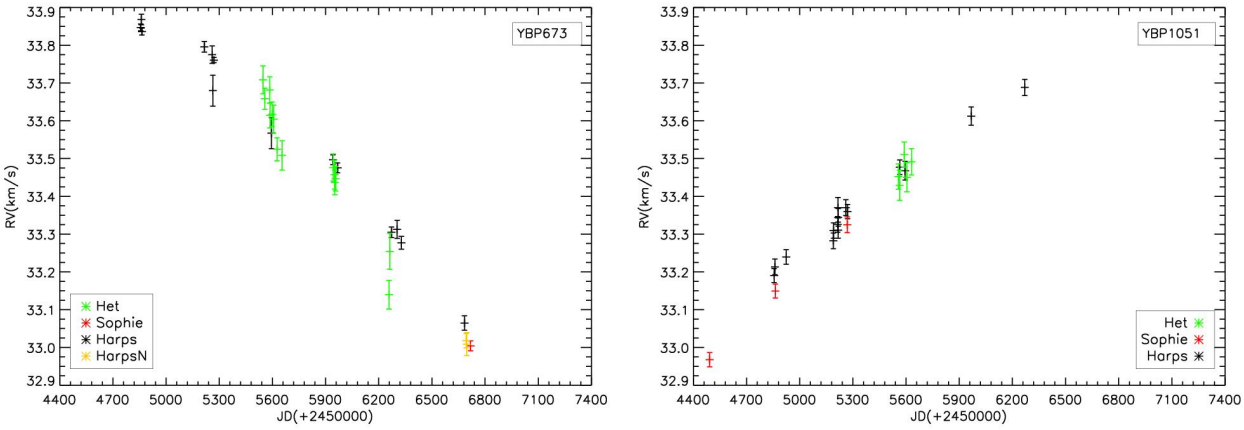

Fig. 3. Stars with large RV or significant linear trends (suspected binaries). Black dots: HARPS measurements, red dots: SOPHIE measurements, orange dots: HARPS-N measurements, and green dots: HRS measurements. RV error bars represent σ_{cor}.

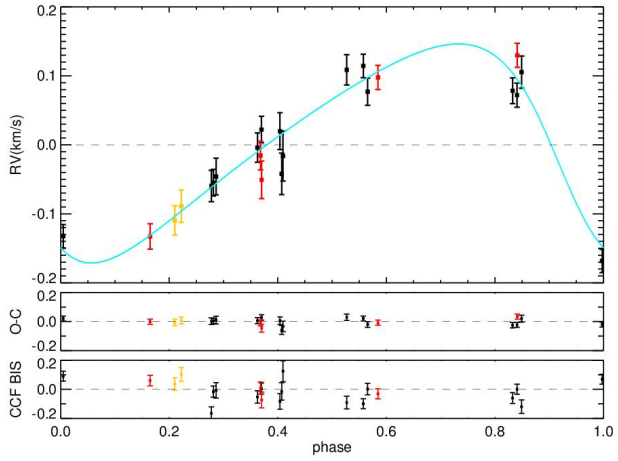

Fig. 4. Phased RV measurements and Keplerian best fit, best-fit residuals, and bisector variation for YBP778. Same symbols as in Fig. 3.

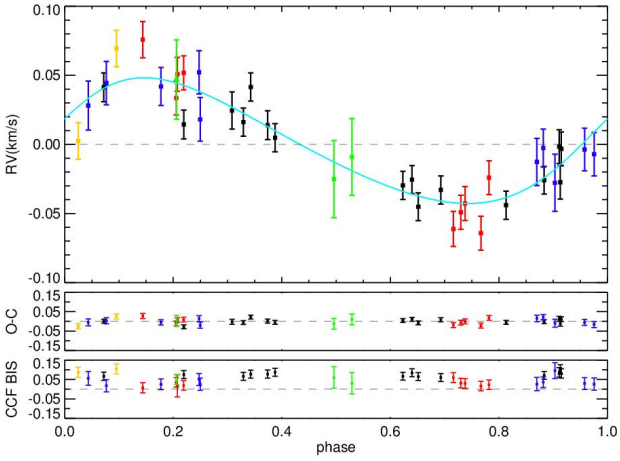

Fig. 5. Phased RV measurements and Keplerian best fit, best-fit residuals, and bisector variation for S978. Same symbols as in Fig. 4. Green dots: HRS measurements, blue dots: CORALIE measurements.

average measurement uncertainty is ~17 m s^{-1} for HARPS and HARPS-N, and ~10 m s^{-1} for SOPHIE. A clear periodic signal can be seen in the periodogram at ~398 days (see Fig. A.3). Thus a single-planet Keplerian model was adjusted to the data, and the best-fit solution corresponds to a signal with a period of 410.4 ± 6.2 days, a semi-amplitude 158.8 ± 21.4 m s^{-1} (see Fig. 4), and an eccentricity of 0.27 ± 0.11. Although no peak is present in the periodograms of the activity index or the bisector span, nor in the CCF FWHM (see Fig. A.3), we detected an anticorrelation between the RVs and the bisector span with a Pearson correlation coefficient of –0.56, and a slight correlation between the radial velocities and the CCF FWHM (see Fig. A.4). The correlation disappears when we consider the RV residual.

We therefore cannot completely exclude stellar activity (magnetic cycles) or a binary companion with low sin(i) as the cause of the RV variation at this point, although in the recent study of Geller et al. (2015), YBP778 is also classified as a single member. Interesting, Pace et al. (2012) noted that this star is significantly underabundant in lithium compared to the lithium abundances as a function of stellar mass for MS stars in M 67. This could argue in favor of the possibility that the star might indeed host a planet (see, e.g., Deal et al. 2015). However, Pace et al. (2012) warned that the distance of this star to the isochrone in the color-magnitude diagram (CMD; ~0.06 mag) could also suggest the presence of a stellar or substellar companion.

S978. The star is a K4 red giant and was observed 40 times over more than five years with HARPS, HRS, SOPHIE, and HARPS-N. The average RV uncertainty is ~3.0 m s^{-1} for HARPS and SOPHIE, ~26.0 m s^{-1} for HRS, and ~8.0 m s^{-1} for HARPS-N. Ten additional RV measurements were obtained with CORALIE between 2003 and 2005, with a mean measurement uncertainty of ~12.0 m s^{-1}. The strongest peak in the periodogram of the RV time series lies at about 510.4 days (see Fig. A.3). Aliases are also present in the periodogram, but at half of the power of the main signal. The bisector inverse slope as well as the activity indicator do not present any significant variation at the period of 510.4 days. We fitted a single-planet Keplerian orbit to this signal (see Fig. 5) and found an orbital solution whose parameters are reported in Table 3. The dispersion of the residuals is σ(O-C) = 12.90 m s^{-1} and the periodogram of the residuals reveals some structures, but no significant peaks (see Fig. A.3).

Several studies indicate that M 67 stars in general have a low level of chromospheric activity. Pace & Pasquini (2004) computed activity levels for M 67 and other clusters. The paper shows that, for instance, the young Hyades and Praesaepe stars on average have a chromospheric emission flux

Table 3. *Top*: stellar parameters of the M 67 stars that are newly found to host planet candidates. *Bottom*: orbital parameters of the planetary companions.

Parameters	YBP401	YBP1194	YBP1514	SAND364	SAND978
α (J2000)	08:51:19.05	08:51:00.81	08:51:00.77	08:49:56.82	08:51:17.48
δ (J2000)	+11:40:15.80	+11:48:52.76	+11:53:11.51	+11:41:33.00	+11:45:22.69
Spec.type	F9V	G5V	G5V	K3III	K4III
m_V [mag]	13.70[a]	14.6[a]	14.77[a]	9.8[b]	9.71[c]
$B-V$ [mag]	0.607[a]	0.626[a]	0.680[a]	1.360[b]	1.370[c]
$M\star$ [$M_\odot$]	1.14 ± 0.02[d]	1.01 ± 0.02[d]	0.96 ± 0.01[d]	1.35 ± 0.05[d]	1.37 ± 0.02[d]
$\log g$ [cgs]	4.30 ± 0.035[f]	4.44 ± 0.05[e]	4.57 ± 0.06[g]	2.20 ± 0.06[h]	1.80 ± 0.09[i]
$T_{\rm eff}$ [K]	6165 ± 64[f]	5780 ± 27[e]	5725 ± 45[g]	4284 ± 9[h]	4200 ± 21[i]
P [days]	4.087 ± 0.003	6.960 ± 0.001	5.118 ± 0.001	120.951 ± 0.453	511.21 ± 2.04
T [JD]	2 456 072.4 ± 0.6	2 455 679.9 ± 0.4	2 455 986.3 ± 0.3	2 456 231.22 ± 4.26	2 456 135.92 ± 21.23
e	0.16 ± 0.08	0.31 ± 0.08	0.27 ± 0.09	0.35 ± 0.10	0.16 ± 0.07
ω [deg]	343.33 ± 62.12	109.16 ± 20.16	328.58 ± 17.78	254.62 ± 15.91	291.68 ± 35.85
K [m s^{-1}]	49.29 ± 5.50	37.35 ± 4.55	50.47 ± 3.90	56.94 ± 4.26	45.48 ± 3.65
$m \sin i$ [$M_{\rm Jup}$]	0.42 ± 0.05	0.33 ± 0.03	0.40 ± 0.35	1.57 ± 0.11	2.18 ± 0.17
γ [km s^{-1}]	33.179 ± 0.004	34.184 ± 0.003	34.058 ± 0.004	33.188 ± 0.019	34.567 ± 0.008
χ^2_{red}	0.97	0.95	0.93	1.08	1.57
σ(O-C) [m s^{-1}]	12.31	11.51	14.24	15.93	12.90

Notes. P: period, T: time at periastron passage, e: eccentricity, ω: argument of periastron, K: semi-amplitude of the RV curve, $m \sin i$: planetary minimum mass, γ: average radial velocity, and σ(O-C): dispersion of the Keplerian fit residuals.

References. [(a)] Yadav et al. (2008). [(b)] Montgomery et al. (1993). [(c)] Sanders (1977). [(d)] Pietrinferni et al. (2004) and Girardi et al. (2000). [(e)] Önehag et al. (2011). [(f)] Pasquini et al. (2008) and Pace et al. (2012). [(g)] Smolinski et al. (2011) and Lee et al. (2008). [(h)] Wu et al. (2011). [(i)] Jacobson et al. (2011).

in the CaII K line of $\langle F'_{\rm K}\rangle \sim 2.1\times10^6$ erg cm^{-2} s^{-1} and $\langle F'_{\rm K}\rangle \sim 2.43\times10^6$ erg cm^{-2} s^{-1}, respectively, while M 67 stars have $\langle F'_{\rm K}\rangle \sim 0.5\times10^6$ erg cm^{-2} s^{-1}, which is not enough to explain the high RV variations we observe. In a survey of the Ca II H and K core strengths of a sample of 60 solar-type stars in M 67, Giampapa et al. (2006) found that the distribution of the HK index (a measure of the strength of the chromospheric H and K cores) is broader than the distribution seen in the contemporary solar cycle. Significant overlap between the HK distribution of the solar cycle and that for the Sun-like stars in M 67 is seen with over 70% of the solar analogs exhibiting Ca II H+K strengths within the range of the modern solar cycle. About ~10% are characterized by high activity in excess of the solar maximum values, while approximately 17% have values of the HK index lower than the solar minimum. Of these, none of the stars showing enhanced activity is present in our final sample. In a following work, the same authors reported the results of the analysis of high-resolution photospheric line spectra obtained with the UVES instrument on the VLT for a subset of 15 solar-type stars in M 67 selected by Giampapa et al. (2006). They found upper limits to the projected rotation velocities that are consistent with solar-like rotation (i.e., $v \sin i \leq 2$–3 km s^{-1}) for objects with Ca II chromospheric activity within the range of the contemporary solar cycle. Two solar-type stars in their sample exhibit chromospheric emission well in excess of even the solar maximum values: Sand747 and Sand1452. In one case, Sand747, the authors found it to be a spectroscopic binary. The other star, Sand1452, was also present in our original sample, but we discovered that the object was also a binary system (Pasquini et al. 2012). Furthermore, of the 15 solar-type stars analyzed in Reiners & Giampapa (2009), seven stars are in common with our sample (in particular our planet-hosts YBP1194 and YBP1514). These objects are slow rotators ($v \sin i \leq 2$ km s^{-1}) and have Sun-like HK values.

Melo et al. (2001) used FEROS spectrograph observations to determine accurate projected rotational velocities $v \sin i$ for a sample of 28 MS, turn-off, and giant stars belonging to M 67. They found that the stars show similar values of $v \sin i$ depending on their position in the CMD. Early MS G stars have a rotational velocity twice higher than the Sun, and they show a possible trend with $(B-V)$ color, with redder colors corresponding to lower $v \sin i$. The stars at the turn-off are the fastest rotators, with $v \sin i$ between 6.3 and 7.6 km s^{-1}, while stars just above the turn-off are already significantly slower, with values between 4.6 and 4.9 km s^{-1}. Along the subgiant branch rotation tends to drop down, and for stars with $(B-V) > 1$ only upper limits can be found, including for the clump stars ($v \sin i \leq 1.5$ km s^{-1}). Most of the stars in this last group are in common with our sample.

To rule out activity-related rotational modulation as the cause of the RV variations in our data, we investigated chromospheric activity by measuring the variations of the core of Hα with respect to the continuum. Using public data with known correlations between activity indicators and RVs, we verified that such correlations could be still recorded at low S/N level of the M 67 spectra. Of our targets, S364 and S978 show a variability in Hα of 2%, YBP1514 and YBP1194 of 3% without significant periodicity and YBP401 of 4%, exhibiting all a very low activity level, while for YBP778 Hα variability is slightly higher, with a value of 7%. The fact that these stars are of solar age and that our research is focused on finding giant planets with an expected RV variability of tens of m s^{-1} makes the contamination by activity negligible.

4.3. Stars with long-term RV variability

The turn-off star S815 shows a peak-to-peak RV variation of the order of ~700 m s^{-1} (see Fig. 6). This star is retained in the single-star sample, although the amplitude of RV values is

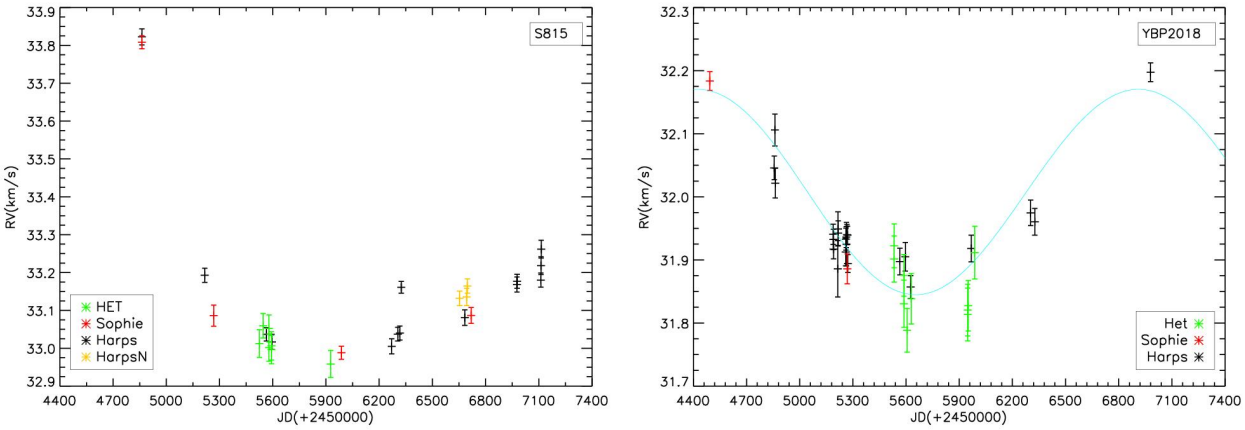

Fig. 6. RV time series for S815 (*left*) and YBP2018 (*right*). For this latter a tentative Keplerian solution is overplotted in blue. Same symbols as in Fig. 3.

possibly too high for a planet. Moreover, the RV measurements would indicate a rather high eccentricity.

The MS star YBP2018 presents peak-to-peak RV variations on the order of ∼400 $\mathrm{m\,s^{-1}}$ and appears to have almost completed one orbit. Figure 6 shows the RV measurements with a tentative Keplerian solution, resulting in an orbiting object with a minimum mass of ∼11.0 M_{Jup} and a period of ∼2487 days. The residuals have an rms of ∼30.0 $\mathrm{m\,s^{-1}}$, but the periodogram of the residuals does not show any clear periodicity. Extensive follow-up over several years is required for this star to understand the nature of the companion candidate.

The MS stars YBP1062 and YBP1137 exhibit a trend in RV measurements of -28.75 $\mathrm{m\,s^{-1}}$/yr and 10.57 $\mathrm{m\,s^{-1}}$/yr. Figures 7 and 8 show the RV time series with the fitted linear trend overlaid. Although the residuals of the linear fit present an RV variability of 33.36 $\mathrm{m\,s^{-1}}$ for YBP1062 and 18.00 $\mathrm{m\,s^{-1}}$ for YBP1137, the periodogram of the residuals for the two stars does not reveal any significant peaks.

The evolved star S488 also shows a high RV variability when compared to the measurement errors but caution is necessary with this star, which is located at the tip on the red giant branch. Dupree et al. (1999) found a strong Ca II emission-line with no visible change in the line asymmetries with time for this star, suggesting the presence of outward mass motions.

When we compute a Lomb-Scargle periodogram, a peak is present at ∼2257 days. At this period, the measurements baseline is not yet long enough to constrain any significant orbital solution. A tentative Keplerian curve is given in Fig. 9 and corresponds to an object with a minimum mass of ∼14.0 M_{Jup} and a period of ∼2332 days. The residuals have an rms amplitude of ∼55 $\mathrm{m\,s^{-1}}$, and when the main signal is removed, the periodogram of the residual shows a peak at ∼95.03 days with a lower significance close to a 0.05 FAP level. Additional observations are needed to draw further conclusions.

5. Planet frequency

A series of simulations based on a Monte Carlo approach have been carried out to determine detection limits for the RV data as a function of planet mass and planet period, and to derive a trustworthy estimate of the occurrence rate of giant planets for our RV survey. Understanding the frequency of different types of planets around stars of different mass can provide important clues about the processes of planet formation and evolution. Moreover, the direct comparison with similar analyses on field star samples can reveal important indications about the influence of the stellar birth environment on the evolution of planetary systems.

In general, the determination of the detection efficiency for an RV survey is based on the ability to recover a planetary signal with a given level of statistical significance. This translates into lower limits on the detectable companion mass as a function of orbital period. Several authors (e.g., Cumming et al. 2008; Howard et al. 2011) have presented statistical analyses of their planet surveys and discussed different methods to derive limits on companion detectability and unbiased distributions for a number of RV planet surveys. They used mainly two approaches: one based on χ^2 and F-tests to detect excess residuals above an assumed Gaussian noise (Lagrange et al. 2009; Sozzetti et al. 2009), and the other approach is based on a periodogram analysis to identify significant periodicity (Cumming 2004; Narayan et al. 2005; Mortier et al. 2012). For our project, the second approach was selected for all the stars with enough data points for a reliable periodogram analysis. For the stars where the periodogram was not feasible because of the combined effect of poor sampling and the small number of observations per star, we evaluated the detection limit using the variability of the RV values with respect to the measurement errors.

5.1. Method

In order to derive the detectability of planetary signals, we computed synthetic datasets, simulating a series of mass and period data pairs (∼10^6 values) of our "potential planets", which are uniformly distributed in a logarithmical mass range of 0.2–10.0 M_{Jup} and in a linear period range of 1.0–1000 days. From the real measurements of each star we retain the observation dates (expressed in Baricentric Julian Date) and the corresponding measurement errors, which we inflated as explained in Sect. 3. For random choices of the planet mass-period pairs and assuming eccentric orbits, we calculated the contribution to the radial velocity amplitude K from a giant planet using the relation

$$K = \left(\frac{2\pi G}{P}\right)^{1/3} \left(\frac{m_{\mathrm{p}} \sin(i)}{M_{\mathrm{Jup}}}\right) \left(\frac{M_\star}{M_\odot}\right)^{-2/3} \left(\frac{1}{\sqrt{1-e^2}}\right), \quad (1)$$

where $M_\star$ is the mass of the host star that we obtained from isochrone fitting. A random distribution of the orbit inclination

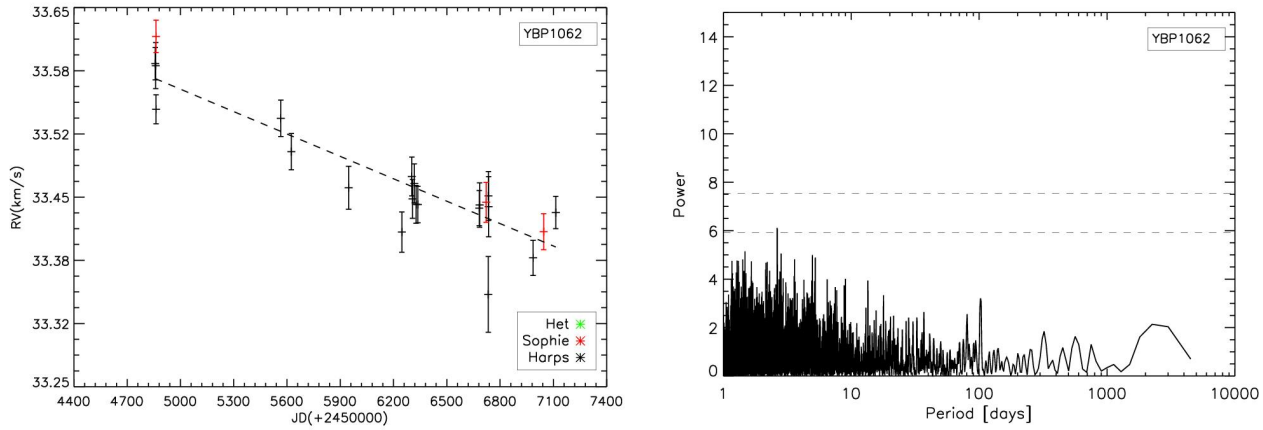

Fig. 7. *Left*: RV time series with the fitted linear trend of YBP1062 overlaid. *Right*: periodogram of the residuals after the RV trend has been removed. Same symbols as in Fig. 3.

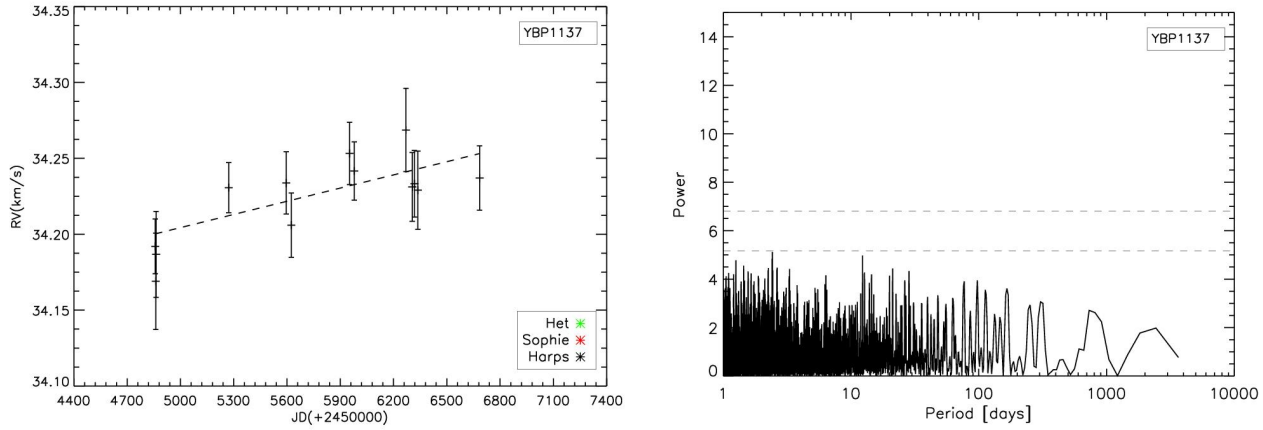

Fig. 8. *Left*: RV time series with the fitted linear trend of YBP1137 overlaid. *Right*: periodogram of the residuals after the RV trend has been removed. Same symbols as in Fig. 3.

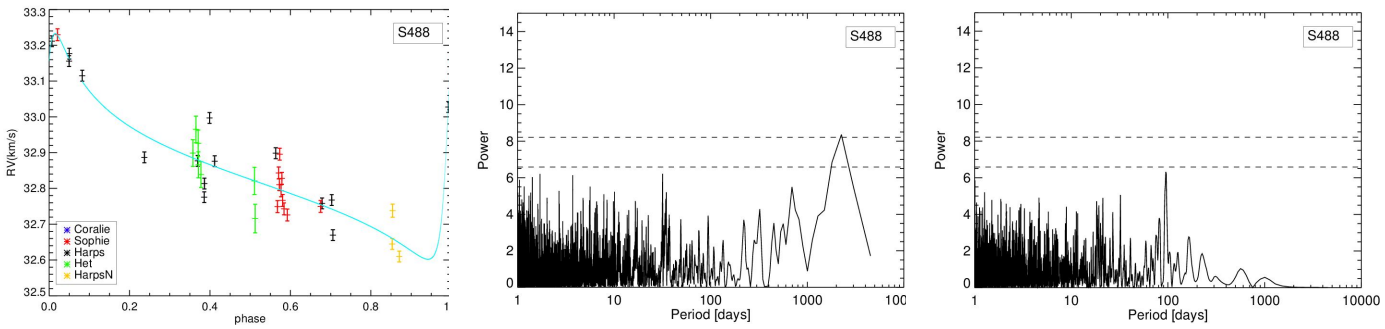

Fig. 9. Phased RV measurements and Keplerian best fit (*left*), periodogram of the RV data (*center*), and periodogram of the residuals for S488.

was also assumed, and the eccentricity e was allowed to vary randomly between $0.0 < e < 0.5$. Then, we derived the synthetic planetary signals following the equation for eccentric Keplerian orbits,

$$V_r(t) = a \cos \nu(t) + b \sin \nu(t) + c, \quad (2)$$

where $a = K \cos \omega$, $b = -K \sin \omega$ and $c = Ke \cos \omega + \gamma$. Here, K is the RV amplitude, e the eccentricity, ω the longitude of periastron, γ the systemic velocity of the system, $\nu(t)$ the true anomaly, which is a function of t, P, and e, and t_0 is the time of periastron passage. The latter was selected randomly in the time span of the observations, and γ was allowed to vary around the RV value of the M 67 cluster obtained in Pasquini et al. (2012). We then degraded the obtained RVs by adding noise corresponding to the actual measurement error of the real observations.

5.1.1. Stars with at least ten data points

A periodogram-based analysis (Scargle 1982) was applied to each synthetic dataset to verify whether the simulated planet was observable. This approach was chosen for all the stars with enough measurements for a reliable periodogram analysis. We

note that this is the same procedure as we applied for the analysis of the RV measurements in Sect. 3.

For a given mass and period values, we considered a planet to be detected if we could obtain a signal from the periodogram analysis that had a power higher than the power associated with a 0.01 FAP. For each star 10^6 trials were used.

In the two-dimensional space of orbital period and planet mass, we consider a grid of period and log-spaced mass cells within which the planet detectability (or detection efficiency, E_{ij}) is individually computed as the number of the potentially detected planets with respect to the total simulated planets in each bin of mass and period. On the base of this analysis, the detection efficiency was carried out for 14 MS stars and 10 evolved stars. Figures A.1 and A.2 show the detection efficiencies for the 24 stars as color contours from 0.0 to 1.0. The red regions have a 100% detectability of planets, and blue regions have low detectability. This means that in red regions (high detectability) all potential planets at the given period and mass would be detected. In the blue regions (low detectability) the detection efficiency decreases, and we are not able to discover their presence at high confidence. In Figs. A.1 and A.2, the resulting distribution of the planet detection efficiency clearly reduced with decreasing planet mass and with increasing period. This is due to the insufficient number of measurements, to the distribution of the observations, and to the weak RV signal. Moreover, windows of poor detectability in the period-mass grid occur for two main reasons: the data structure (number of observations and phase coverage), and the one-year seasonal period that affects any ground-based observing program.

5.1.2. Stars with poor sampling and few observations

In order to take into account the contribution of stars with poor sampling and few observations, we derived the number of detectable planets using the measurements rms. We considered the same grid of period and log-spaced mass cells as described in Sect. 5.1. In each cell of the mass-period grid, we evaluated the average rms of the synthetic radial velocities for the simulated planets ($\mathrm{RMS_{sim}}$). We set our detection threshold by identifying for each star the mass-period cells with synthetic average RV variation more than three times higher than the estimated errors ($\mathrm{RMS_{sim}} > 3\sigma_{\mathrm{corr}}$) of our real measurements. Inflated measurements errors were used in the analysis.

All potential planets with $\mathrm{RMS_{sim}}$ smaller than $3\sigma_{\mathrm{corr}}$ were instead considered undetectable.

Finally, we folded the results of all the stars by obtaining the mass-period cell-matrix M. The value for each M_{ij} cell represents the total number of poorly sampled stars for which planets in that cell would be detected.

As an example, the detection regions for a star of the sample derived using the RV rms analysis is shown in Fig. 10. In the red area the rms of the simulated RV values ($\mathrm{RMS_{sim}}$) is more than three times higher than the real measurements error (σ_{corr}): all hypothetical planets in this mass-period range would be detected. In the blue ruled area the rms of the simulated RV values ($\mathrm{RMS_{sim}}$) is lower than $3\sigma_{\mathrm{corr}}$: potential planets in this mass-period range cannot be detected with our observations.

5.1.3. Planetary occurrence

We computed the planet occurrence rate $\gamma(P, M)$, that is, the fraction of stars of our survey that are orbited by giant planets in the selected period-mass ranges, using the following formalism.

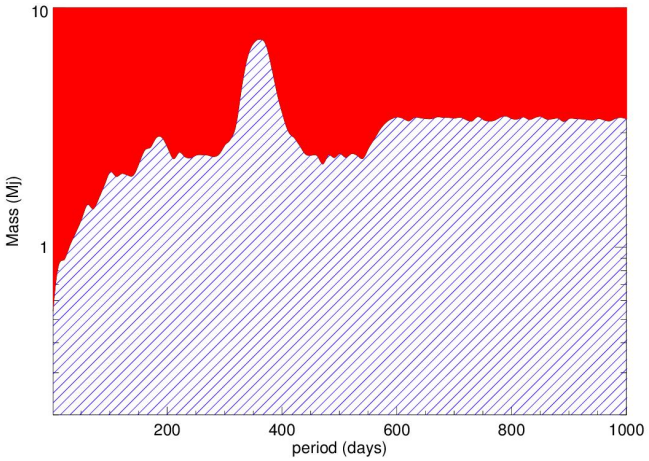

Fig. 10. Planet detection regions for a star of the sample derived using the RV rms analysis. Red area: the rms of the simulated RV values is more than three times higher than the real measurement error, thus all potential planets can be detected. Blue ruled area: the rms of the simulated RV values is lower than three times the real measurement errors. Potential planets in this mass-period range cannot be detected with our observations.

Considering the 24 stars analyzed with the Lomb-Scargle method, we derived the completeness, expressed as detectable planetary number, $R_{\star,k}$, for each k star. First we weighted the calculated detection efficiency with the mass-period distribution of planets derived from the relation of Cumming et al. (2008): $\mathrm{d}f \propto M^{-0.31\pm0.2} P^{0.26\pm0.1} \mathrm{d}\log M \mathrm{d}\log P$. Therefore we defined

$$R_{\star,k} = c \sum_{ij}^{N\mathrm{bins}} E_{ij} \cdot D_{ij}, \tag{3}$$

where the sum is evaluated over the entire mass-period bins. E_{ij} corresponds to the detection efficiency for each period-mass cell, D_{ij} represents the mass-period distribution of planets within each bin and is calculated by

$$D_{ij} = \int_{\mathrm{bin}} M^{-0.31\pm0.2} P^{0.26\pm0.1} \mathrm{d}\log M \mathrm{d}\log P. \tag{4}$$

The normalization constant c is defined conveniently inside our mass-period domain by the relation

$$1 = c \int_{1.0}^{1000} \int_{0.2}^{10} M^{-0.31\pm0.2} P^{0.26\pm0.1} \mathrm{d}\log M \mathrm{d}\log P. \tag{5}$$

Finally, we summed the values obtained from the analysis of all the MS and giant stars (G) as

$$R_{\mathrm{MStot}} = \sum_{\mathrm{MS\ stars}} R_{\star k}, \quad R_{\mathrm{Gtot}} = \sum_{\mathrm{G\ stars}} R_{\star k}. \tag{6}$$

R_{MStot} and R_{Gtot} can be interpreted as the number of planets that would be detected if every star in the sample were hosting a planet. We imposed the result to be proportional to the number of real detected planets in the seven-year-long RV survey (three MS and two giant stars):

$$3 = \gamma_{\mathrm{MS}} R_{\mathrm{MStot}}, \quad 2 = \gamma_{\mathrm{G}} R_{\mathrm{Gtot}}. \tag{7}$$

Therefore, the proportional constants γ_{MS} and γ_{G} represent an estimate of the planet occurrence rate of our survey for the MS and G stars respectively. In the analysis, turn-off stars with

$12.5 \leq M_V \leq 13.5$ and $0.540 \leq (B-V) \leq 0.640$ were considered part of the MS sample, and the others were considere part of the G sample.

Subsequently, we decided to include a correction for the total detection efficiency to take the contribution of the stars with few observations and poor sampling into account in computing the planet occurrence rate.

Two cases were evaluated.

In the first, the planet occurrence among the MS stars ($N_{\rm MS}$ = 14) and the evolved stars ($N_{\rm G}$ = 10) was rescaled with the ratio of $N_{\rm MS}$ or $N_{\rm G}$ over the total number of stars considered in the analysis: 14 of 56 for the MS and 10 of 20 for the giant stars. This corresponds to the more conservative approach, where all the stars with few observations do not have a companion.

In the second case, we instead decided to rescale the detection efficiency for each cell E_{ij} as

$$E'_{ij} = \left(\frac{M_{ij} + N_{\rm stars}}{N_{\rm stars}}\right) \cdot E_{ij}, \quad (8)$$

where M_{ij} is the number of stars with potentially detectable planets for each mass-period cell calculated using the method based on the RV value rms. In this case, only stars with few observations and poor sampling were considered. $N_{\rm stars}$ is the number of the stars with potentially detectable planets obtained with the periodogram-based analysis.

5.2. Discussion

When we consider only the 14 MS and the 10 evolved stars described in the previous section, the planet occurrence in our survey results in the values of $\gamma_{\rm MS} \sim 58.3^{+56.4}_{-31.1}\%$ for the MS and $\gamma_{\rm G} \sim 43.8^{+57.2}_{-28.5}\%$ for giants. The errors on the number of found planets are calculated following the prescription of Gehrels (1986). Combining the values for MS and giants gives a total occurrence rate of $\gamma_{\rm tot} \sim 51.5^{+35.0}_{-22.7}\%$. These 24 objects represent the fraction of the stars with a detection efficiency high enough for the number of observations to observe giant planets in the selected range of mass and period (see Figs. A.1 and A.2).

Applying then the correction for the detectability based on those stars that have fewer observations, we obtained the following values for the two considered approaches. In the more conservative case, without further detections, the planet occurrence becomes $\sim 14.6^{+14.1}_{-8.0}\%$ for the MS stars, $\sim 21.9^{+28.6}_{-14.2}\%$ for the giant stars, and $\sim 16.3^{+11.0}_{-7.0}\%$ for the whole sample.

In the more general case, the procedure previously described instead gives a giant planet occurrence of $\sim 15.8^{+15.3}_{-8.4}\%$ for the MS stars and $\sim 23.0^{+29.9}_{-15.0}\%$ for the evolved stars. When referring to the whole sample, the occurrence is $\sim 18.0^{+12.0}_{-8.0}\%$.

The values from the latter more general analysis are finally considered as the final results of our study. Interestingly, they are similar to the results of RV surveys around FGK field stars that show exoplanet rates of ~13% for Jupiter-mass stars in approximately the same range of periods (Mayor et al. 2011; Cumming et al. 2008).

Moreover, when we investigated only the frequency of hot Jupiters around MS stars of our survey and exactly repeated the procedure described in the previous sections, but focusing on objects with periods shorter than 10 days, we found a hot Jupiter occurrence rate of $\sim 5.1^{+4.9}_{-3.0}\%$ for the conservative approach and of $\sim 5.7^{+5.5}_{-3.0}\%$ for the more general case. These values appear to be higher than what is observed in field stars (Wright et al. 2012; Howard et al. 2011). About this argument in particular, we refer to the discussion presented in our parallel work (Brucalassi et al. 2016). We pointed out in that paper that the high rate of hot Jupiters could be favored by a formation scenario dominated by strong encounters with other stars or binary companions and subsequent planet-planet scattering, as predicted by N-body simulations. In this context, we should consider that rescaling the actual M 67 detectability with the mass-period distribution derived by Cumming et al. (2008) for the field stars as done in the previous section could produce a biased result. However, future investigations and a larger number of planet detections in stars cluster are required to assess this hypothesis.

Finally, it is worth to point out that we did not find any clear detection of long-period giant planets around MS stars, possibly because the sensitivity of our survey decreases heavily for long-period planets. However, the recent discovery in the Praesepe cluster of a second massive outer planet around Pr0211 that hosts a close hot Jupiter on a slightly eccentric orbit (Malavolta et al. 2016) suggests that further long-term monitoring could yield indications of interesting discoveries in OCs.

6. Summary and conclusion

We have presented the results of a long-term search program for giant planets in the solar-age, solar-metallicity open cluster M 67.

Five different instruments were used, and after finding proper zero-point corrections to HARPS, 1145 observations for 88 stars were analyzed.

The problem of combining long-term precision RV data from different instruments complicates the analysis. Zero-points offsets were derived with a limited precision, which leads to a loss of sensitivity for trends and long periods. However, this problem quite frequently occurs in long-term surveys because spectrographs receive upgrades or survey projects are transferred to new instruments. Long-term access to the same telescope or instrument configuration is therefore quite important for this type of studies.

Five stars of our sample are found to host planets. One of them (YBP401) has recently been presented in Brucalassi et al. (2016), and in that work we have refined the parameters, based on new measurements, of other two planets announced previously around YBP1194 and YBP1514 (Brucalassi et al. 2014). The other planet-host candidate S978 was discussed in this paper. We have no clear additional planet detection in our sample, but some promising or controversial cases such as YBP778 and YBP2018 call for follow-up observations. Fourteen new binaries were identified and added to the catalog of known M 67 binaries that has been created in Paper I (Pasquini et al. 2012). Moreover, we see trends in S1062 and S1137, and large RV scattering is exhibited by S815 and S488, which might be explained by stellar companions or substellar objects. However, stellar chromospherical activity and magnetic cycles may cause RV variations that might be mistaken as companions. Activity indicators such as the Ca II H&K lines, Hα, and the bisector span are fundamental to verify claimed planets from RV variability.

We provided an estimate of the planet occurrence rate $\gamma(P, M)$, that is, the fraction of stars of our survey that is orbited by Jupiter planets in the ranges of period between 1.0 day and 1000 days and has a planet mass between 0.2 $M_{\rm J}$ and 10.0 $M_{\rm J}$. Although one of the main problems of this survey was the poor and sparse sampling and the small number of observations per star, which complicates the statistical analysis and increases the uncertainty on the frequency of Jupiters in our survey, we find

a total occurrence rate of Jupiter-mass planets in the M 67 sample of $\sim 18.0^{+12.0}_{-8.0}$% (precisely $\sim 15.8^{+15.3}_{-8.4}$% for the MS stars and $\sim 23.0^{+29.9}_{-15.0}$% for the evolved stars). It is worth noting that on average we need a minimum number of 20 observations per star to exclude Jupiter-mass planets at high confidence when a periodogram analysis is applied.

The Jupiter-mass planets in our sample imply that our results are consistent with the planet frequency of much larger surveys carried out for field star samples. For example, from the ELODIE survey, Naef et al. (2005) estimated that a fraction of 7.5 ± 1.5% stars host giant planets with periods shorter than 10 yr, while Cumming et al. (2008) derived a frequency of 12 ± 1.6% from the Keck survey and Mayor et al. (2011) 13.9 ± 1.7% from the HARPS/CORALIE survey.

As a general conclusion, our simulation study seems to confirm the recent finding (Meibom et al. 2013) that the frequency of massive planets around stars of open clusters agrees with the frequency of these planets around field stars.

However, we note that when we only investigate the frequency of hot Jupiters around MS stars of our survey, we find a hot Jupiter occurrence rate ($\sim 5.7^{+5.5}_{-3.0}$%) that is substantially higher than what is observed in field stars (see also Brucalassi et al. 2016).

We have shown that the search for planets in open clusters is a powerful test benchmark for the theory of planet formation and stellar evolution. The new generation of spectrographs such as ESPRESSO (Pasquini et al. 2009) will extend this search more effectively. It is clear, however, that to efficiently perform a planet search survey in star clusters, a multi-object capability, even with relatively low multiplex (10–50), is desirable. Unfortunately, no such facility is currently planned.

Acknowledgements. L.P. acknowledges the Visiting Researcher program of the CNPq Brazilian Agency, at the Fed. Univ. of Rio Grande do Norte, Brazil. RPS thanks ESO DGDF, the whole GAPS-TNG community, the Hobby Eberly Telescope (HET) project, the PNPS and PNP of INSU – CNRS for allocating the observations and the technical support. M.T.R. received support from PFB06 CATA (CONICYT). We are grateful to Gaspare Lo Curto and Michele Cappetta for the support in data reduction analysis and helpful discussions.

References

Baranne, A., Queloz, D., Mayor, M., et al. 1996, A&AS, 119, 373
Baumann, P., Ramírez, I., Meléndez, J., et al. 2010, A&A, 519, A87
Bouchy, F., & Sophie Team 2006, in Tenth Anniversary of 51 Peg-b, eds. L. Arnold, F. Bouchy, & C. Moutou, 319
Brucalassi, A., Pasquini, L., Saglia, R., et al. 2014, A&A, 561, L9
Brucalassi, A., Pasquini, L., Saglia, R., et al. 2016, A&A, 592, L1
Cai, M. X., Spurzem, R., & Kouwenhoven, M. B. N. 2016, IAU Symp., 312, 235
Cappetta, M., Saglia, R. P., Birkby, J. L., et al. 2012, MNRAS, 427, 1877
Cumming, A. 2004, MNRAS, 354, 1165
Cumming, A., Butler, R. P., Marcy, G. W., et al. 2008, PASP, 120, 531
Davies, M. B., Adams, F. C., Armitage, P., et al. 2014, Protostars and Planets VI, 787
Dawson, R. I., & Murray-Clay, R. A. 2013, ApJ, 767, L24
Deal, M., Richard, O., & Vauclair, S. 2015, A&A, 584, A105
Dong, S., Katz, B., & Socrates, A. 2014, ApJ, 781, L5
Dupree, A. K., Whitney, B. A., & Pasquini, L. 1999, ApJ, 520, 751
Gehrels, N. 1986, ApJ, 303, 336
Geller, A. M., Latham, D. W., & Mathieu, R. D. 2015, AJ, 150, 97
Giampapa, M. S., Hall, J. C., Radick, R. R., & Baliunas, S. L. 2006, ApJ, 651, 444
Gilliland, R. L., Brown, T. M., Guhathakurta, P., et al. 2000, ApJ, 545, L47
Girardi, L., Bressan, A., Bertelli, G., & Chiosi, C. 2000, A&AS, 141, 371
González Hernández, J. I., Israelian, G., Santos, N. C., et al. 2010, ApJ, 720, 1592
González Hernández, J. I., Delgado-Mena, E., Sousa, S. G., et al. 2013, in New Quests in Stellar Astrophysics III: A Panchromatic View of Solar-Like Stars, With and Without Planets, eds. M. Chavez, E. Bertone, O. Vega, & V. De la Luz, ASP Conf. Ser., 472, 97
Hekker, S., Snellen, I. A. G., Aerts, C., et al. 2008, A&A, 480, 215
Horne, J. H., & Baliunas, S. L. 1986, ApJ, 302, 757
Howard, A. W., Marcy, G. W., Bryson, S. T., & et al. 2011, ApJ, 730, 10
Jacobson, H. R., Pilachowski, C. A., & Friel, E. D. 2011, AJ, 142, 59
Johnson, J. A., Aller, K. M., et al. 2010, PASP, 122, 905
Lagrange, A.-M., Desort, M., Galland, F., Udry, S., & Mayor, M. 2009, A&A, 495, 335
Lee, Y. S., Beers, T. C., Sivarani, T., et al. 2008, AJ, 136, 2050
Li, G., & Adams, F. C. 2015, MNRAS, 448, 344
Lovis, C., & Mayor, M. 2007, A&A, 472, 657
Malavolta, L., Nascimbeni, V., Piotto, G., et al. 2016, A&A, 588, A118
Malmberg, D., Davies, M. B., & Heggie, D. C. 2011, MNRAS, 411, 859
Mathieu, R. D., Latham, D. W., Griffin, R. F., & Gunn, J. E. 1986, AJ, 92, 1100
Mayor, M., Pepe, F., Queloz, D., et al. 2003, The Messenger, 114, 20
Mayor, M., Marmier, M., Lovis, C., et al. 2011, ArXiv e-prints [arXiv:1109.2497]
Meibom, S., Torres, G., Fressin, F., et al. 2013, Nature, 499, 55
Meléndez, J., Asplund, M., Gustafsson, B., & Yong, D. 2009, ApJ, 704, L66
Melo, C. H. F., Pasquini, L., & De Medeiros, J. R. 2001, A&A, 375, 851
Mermilliod, J.-C., & Mayor, M. 2007, A&A, 470, 919
Montgomery, K. A., Marschall, L. A., & Janes, K. A. 1993, AJ, 106, 181
Mortier, A., Santos, N. C., Sozzetti, A., et al. 2012, A&A, 543, A45
Naef, D., Mayor, M., Beuzit, J.-L., et al. 2005, in 13th Cambridge Workshop on Cool Stars, Stellar Systems and the Sun, eds. F. Favata, G. A. J. Hussain, & B. Battrick, ESA SP, 560, 833
Narayan, R., Cumming, A., & Lin, D. N. C. 2005, ApJ, 620, 1002
Nascimbeni, V., Bedin, L. R., Piotto, G., De Marchi, F., & Rich, R. M. 2012, A&A, 541, A144
Önehag, A., Korn, A., Gustafsson, B., et al. 2011, A&A, 528, A85
Önehag, A., Gustafsson, B., & Korn, A. 2014, A&A, 562, A102
Pace, G., & Pasquini, L. 2004, A&A, 426, 1021
Pace, G., Pasquini, L., & François, P. 2008, A&A, 489, 403
Pace, G., Castro, M., Meléndez, J., Théado, S., & do Nascimento, J. J.-D. 2012, A&A, 541, A150
Pasquini, L., & Pallavicini, R. 1991, A&A, 251, 199
Pasquini, L., Biazzo, K., Bonifacio, P., et al. 2008, A&A, 489, 677
Pasquini, L., Manescau, A., Avila, G., et al. 2009, in Science with the VLT in the ELT Era, ed. A. Moorwood, 395
Pasquini, L., Brucalassi, A., Ruiz, M. T., et al. 2012, A&A, 545, A139
Pepe, F., Mayor, M., Galland, F., et al. 2002, A&A, 388, 632
Perruchot, S., Bouchy, F., et al. 2011, in SPIE Conf. Ser., 8151
Pietrinferni, A., Cassisi, S., Salaris, M., & Castelli, F. 2004, ApJ, 612, 168
Queloz, D., Henry, G. W., Sivan, J. P., et al. 2001, A&A, 379, 279
Quinn, S. N., White, R. J., Latham, D. W., et al. 2012, ApJ, 756, L33
Quinn, S. N., White, R. J., Latham, D. W., et al. 2014, ApJ, 787, 27
Ramírez, I., Asplund, M., Baumann, P., Meléndez, J., & Bensby, T. 2010, A&A, 521, A33
Randich, S., Sestito, P., Primas, F., et al. 2006, A&A, 450, 557
Reiners, A., & Giampapa, M. S. 2009, ApJ, 707, 852
Sanders, W. L. 1977, A&AS, 27, 89
Santerne, A., Díaz, R. F., Moutou, C., et al. 2012, A&A, 545, A76
Santos, N. C., Gomes da Silva, J., Lovis, C., & Melo, C. 2010, A&A, 511, A54
Sato, B., Izumiura, H., Toyota, E., et al. 2007, ApJ, 661, 527
Scargle, J. D. 1982, ApJ, 263, 835
Setiawan, J., Pasquini, L., da Silva, L., et al. 2004, A&A, 421, 241
Shara, M. M., Hurley, J. R., & Mardling, R. A. 2016, ApJ, 816, 59
Smolinski, J. P., Lee, Y. S., Beers, T. C., et al. 2011, AJ, 141, 89
Sozzetti, A., Torres, G., Latham, D. W., et al. 2009, ApJ, 697, 544
Spurzem, R., Giersz, M., Heggie, D. C., & Lin, D. N. C. 2009, ApJ, 697, 458
Tull, R. G., MacQueen, P. J., Good, J., Epps, H. W., & HET HRS Team 1998, BAAS, 30, 1263
Wright, J. T., & Howard, A. W. 2009, ApJS, 182, 205
Wright, J. T., Marcy, G. W., Howard, A. W., et al. 2012, ApJ, 753, 160
Wu, Y., Luo, A.-L., Li, H.-N., et al. 2011, RA&A, 11, 924
Yadav, R. K. S., Bedin, L. R., Piotto, G., et al. 2008, A&A, 484, 609

Appendix A: Accompanying plots and table

Table A.1. Observed targets in M 67.

Object	$B-V$	M_V	H	S	C	HET	H-N	TOT	RV(km s^{-1})	$\sigma_{\rm obs}$(km s^{-1})	$\sigma_{\rm cor}$(km s^{-1})	σ_{RV}(km s^{-1})
YBP219	**0.570**	**13.6**	**6**	**5**	**0**	**0**	**0**	**11**	**33.714**	**0.016**	**0.022**	**0.323**
YBP266	0.570	13.6	11	3	0	0	1	15	33.774	0.017	0.022	0.031
YBP285	0.663	14.5	7	2	0	0	0	9	34.397	0.016	0.022	0.019
YBP288	**0.637**	**13.9**	**1**	**2**	**0**	**0**	**0**	**3**	**37.691**	**0.010**	**0.018**	**1.299**
YBP291	0.570	13.5	23	3	0	0	0	26	32.521	0.017	0.022	0.026
YBP349	0.636	14.3	11	0	0	0	0	11	35.048	0.014	0.020	0.023
YBP350	0.561	13.6	11	2	0	0	0	13	33.227	0.015	0.021	0.020
YBP401	0.566	13.7	19	5	0	0	2	26	33.178	0.015	0.021	0.035
YBP473	0.658	14.4	7	0	0	0	0	7	33.266	0.016	0.022	0.023
YBP587	0.605	14.1	6	2	0	0	0	8	33.188	0.013	0.020	0.028
YBP613	0.612	13.3	10	4	0	0	0	14	33.565	0.015	0.021	0.020
YBP637	0.661	14.5	5	2	0	0	0	7	34.801	0.014	0.020	0.019
YBP673	**0.665**	**14.4**	**14**	**1**	**0**	**14**	**2**	**31**	**33.496**	**0.026**	**0.030**	**0.249**
YBP689	0.622	13.1	10	2	0	3	0	15	33.650	0.017	0.022	0.044
YBP750	0.598	13.6	4	1	0	0	0	5	34.251	0.014	0.020	0.011
YBP769	**0.665**	**14.4**	**2**	**1**	**0**	**0**	**0**	**3**	*CCF Double peak*			
YBP778	0.582	13.1	15	4	0	0	2	21	34.288	0.016	0.022	0.090
YBP809	0.696	15.0	5	0	0	0	0	5	32.864	0.011	0.019	0.011
YBP851	**0.617**	**14.4**	**3**	**1**	**0**	**0**	**0**	**4**	**33.759**	**0.010**	**0.018**	**1.417**
YBP911	**0.673**	**14.6**	**2**	**0**	**0**	**0**	**0**	**2**	**33.738**	**0.020**	**0.025**	**0.703**
YBP988	0.598	14.2	5	1	0	0	0	6	32.862	0.013	0.020	0.016
YBP1032	0.598	14.4	6	0	0	0	0	6	34.913	0.013	0.020	0.013
YBP1036	0.690	15.0	15	0	0	0	0	15	34.025	0.015	0.021	0.025
YBP1051	**0.595**	**14.1**	**15**	**3**	**0**	**5**	**0**	**23**	**33.364**	**0.016**	**0.022**	**0.156**
YBP1062	0.626	14.5	19	3	0	0	0	22	33.462	0.017	0.022	0.067
YBP1067	**0.642**	**14.6**	**7**	**0**	**0**	**2**	**0**	**9**	**33.667**	**0.019**	**0.024**	**1.030**
YBP1075	0.633	13.7	11	1	0	0	1	13	33.858	0.014	0.020	0.034
YBP1088	0.618	14.5	8	0	0	0	0	8	33.434	0.014	0.020	0.022
YBP1090	**0.650**	**13.8**	**2**	**1**	**0**	**0**	**0**	**3**	**35.186**	**0.021**	**0.025**	**1.265**
YBP1101	0.661	14.7	4	1	0	0	0	5	33.484	0.015	0.021	0.029
YBP1129	0.583	14.2	4	1	0	0	0	5	34.479	0.009	0.018	0.009
YBP1137	0.657	14.9	13	0	0	0	0	13	34.227	0.018	0.023	0.031
YBP1194	0.626	14.6	16	6	0	5	2	29	34.189	0.017	0.022	0.027
YBP1197	0.565	13.3	10	0	0	0	0	10	34.591	0.017	0.022	0.015
YBP1247	0.568	14.1	5	1	0	0	0	6	32.966	0.013	0.020	0.014
YBP1303	0.636	14.6	4	1	0	0	0	5	33.395	0.017	0.022	0.019
YBP1304	**0.723**	**14.7**	**2**	**1**	**0**	**0**	**0**	**3**	**32.512**	**0.019**	**0.024**	**2.670**
YBP1315	**0.693**	**14.3**	**5**	**2**	**0**	**6**	**0**	**13**	**34.885**	**0.022**	**0.026**	**0.801**
YBP1334	0.639	14.4	6	1	0	0	0	7	33.066	0.014	0.020	0.021
YBP1387	0.585	14.1	5	1	0	0	0	6	34.059	0.012	0.019	0.017
YBP1392	0.675	14.8	8	1	0	0	0	6	34.556	0.016	0.022	0.023
YBP1458	0.698	15.0	6	0	0	0	0	6	33.417	0.013	0.020	0.015
YBP1496	0.556	13.9	8	1	0	0	0	9	34.786	0.015	0.021	0.017
YBP1504	0.584	14.2	4	1	0	0	0	5	33.761	0.013	0.020	0.018
YBP1514	0.680	14.8	17	5	5	0	0	27	34.048	0.018	0.023	0.036
YBP1587	0.600	14.2	11	1	0	0	1	13	33.446	0.011	0.019	0.035
YBP1622	0.591	14.2	6	0	0	0	0	6	33.951	0.012	0.019	0.015
YBP1716	**0.619**	**13.3**	**5**	**1**	**0**	**7**	**0**	**13**	**36.205**	**0.010**	**0.018**	**0.651**
YBP1722	0.560	14.1	10	1	0	5	1	17	34.483	0.018	0.023	0.025
YBP1735	0.620	14.3	5	0	0	0	0	5	33.976	0.013	0.020	0.014
YBP1758	**0.653**	**13.2**	**2**	**1**	**0**	**0**	**0**	**3**	**29.653**	**0.011**	**0.019**	**1.521**
YBP1768	0.615	14.4	3	0	0	0	0	3	34.497	0.012	0.019	0.003
YBP1787	0.626	14.5	8	1	0	0	0	9	34.065	0.014	0.020	0.016
YBP1788	0.622	14.4	8	0	0	0	0	8	34.162	0.014	0.020	0.042

Notes. Object name, basic stellar parameters, number of observations for each instrument (H: HARPS, S: SOPHIE, C: CORALE, HET: HRS at Het, H-N: HARPS-N), total number of observations, mean stellar RV, average measurements error, average corrected measurements error, observed RV dispersion. Binary candidates are indicated in bold face.

Table A.1. continued.

Object	$B-V$	M_V	H	S	C	HET	H-N	TOT	RV(km s^{-1})	$\sigma_{\rm obs}$(km s^{-1})	$\sigma_{\rm cor}$(km s^{-1})	σ_{RV}(km s^{-1})
YBP1852	0.572	14.0	7	1	0	0	0	8	32.914	0.013	0.020	0.018
YBP1903	0.648	14.7	5	0	0	0	0	5	33.390	0.017	0.022	0.023
YBP1948	0.571	14.0	4	1	0	0	0	5	33.333	0.012	0.019	0.011
YBP1955	0.589	14.2	6	1	0	0	0	7	33.212	0.013	0.020	0.021
YBP2018	0.631	14.6	22	2	0	7	0	31	31.991	0.020	0.025	0.089
S364	1.360	9.8	14	6	7	5	0	32	33.198	0.010	0.018	0.042
S488	1.550	8.9	15	11	0	8	3	37	32.861	0.012	0.019	0.156
S602	0.512	12.9	6	4	0	7	0	17	33.894	0.018	0.023	0.047
S610	0.493	12.9	5	1	0	5	0	11	33.371	0.024	0.027	0.056
S657	0.559	12.3	8	0	0	0	0	8	33.234	0.008	0.017	0.015
S731	0.516	13.1	10	1	0	0	0	11	33.097	0.012	0.019	0.021
S815	0.497	12.9	14	4	0	7	3	28	34.139	0.019	0.024	0.207
S978	1.332	9.7	16	9	10	3	2	40	34.577	0.010	0.018	0.043
S989	1.048	11.4	8	1	8	3	0	20	34.795	0.019	0.024	0.024
S1001	0.759	12.4	3	1	0	0	0	4	33.409	0.007	0.017	0.024
S1010	1.069	10.5	7	3	6	0	0	16	33.746	0.009	0.018	0.025
S1016	1.098	10.3	7	11	0	0	0	18	33.872	0.004	0.016	0.072
S1054	0.859	11.2	8	1	9	0	0	18	33.500	0.015	0.021	0.025
S1074	1.111	10.4	3	1	9	0	0	13	34.139	0.014	0.020	0.042
S1084	1.086	10.5	15	1	6	5	0	27	33.900	0.007	0.017	0.021
S1230	0.524	13.1	4	0	0	0	0	4	33.773	0.013	0.020	0.005
S1254	0.999	11.5	10	3	5	0	0	18	32.867	0.013	0.020	0.058
S1271	0.506	12.9	11	2	0	0	0	13	33.648	0.016	0.022	0.023
S1279	1.081	10.6	7	2	7	0	0	16	33.384	0.010	0.018	0.021
S1288	1.016	11.3	5	1	6	0	0	12	33.454	0.020	0.025	0.040
S1293	0.565	12.1	13	10	0	7	0	30	34.094	0.010	0.018	0.042
S1305	0.945	12.2	14	2	0	6	0	22	33.964	0.011	0.019	0.020
S1316	1.077	10.6	9	2	6	4	0	21	32.860	0.012	0.019	0.028
S1402	1.109	10.9	4	1	0	0	0	5	33.781	0.007	0.017	0.008
S1479	0.682	10.5	6	1	6	0	0	13	34.319	0.011	0.019	0.013
S1557	1.249	10.1	13	13	6	4	1	37	33.797	0.010	0.018	0.138
S1583	**0.665**	**14.4**	**2**	**1**	**0**	**0**	**0**	**3**	*CCF Double peak*			
S1592	1.032	10.5	4	2	8	0	0	14	33.639	0.011	0.018	0.024
S1607	0.548	12.7	12	6	0	2	2	22	33.391	0.013	0.019	0.062

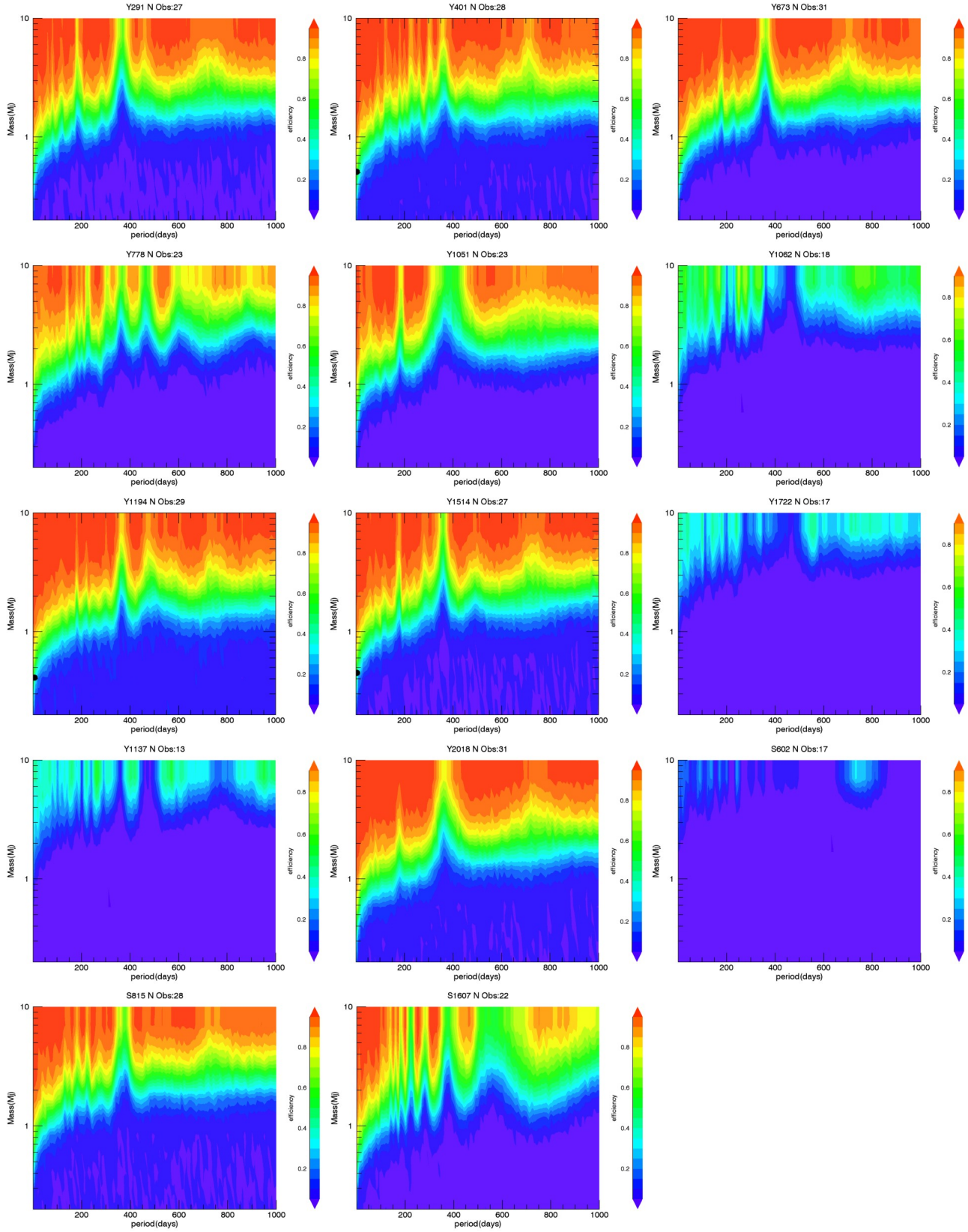

Fig. A.1. Contours of the planet detection efficiency for the MS stars in the domains of 1–1000 days for planet period and 0.2–10 M_J for planet mass. A 0.01 FAP level has been used as detection planet threshold in the periodogram analysis. A filled circle indicates the planet position.

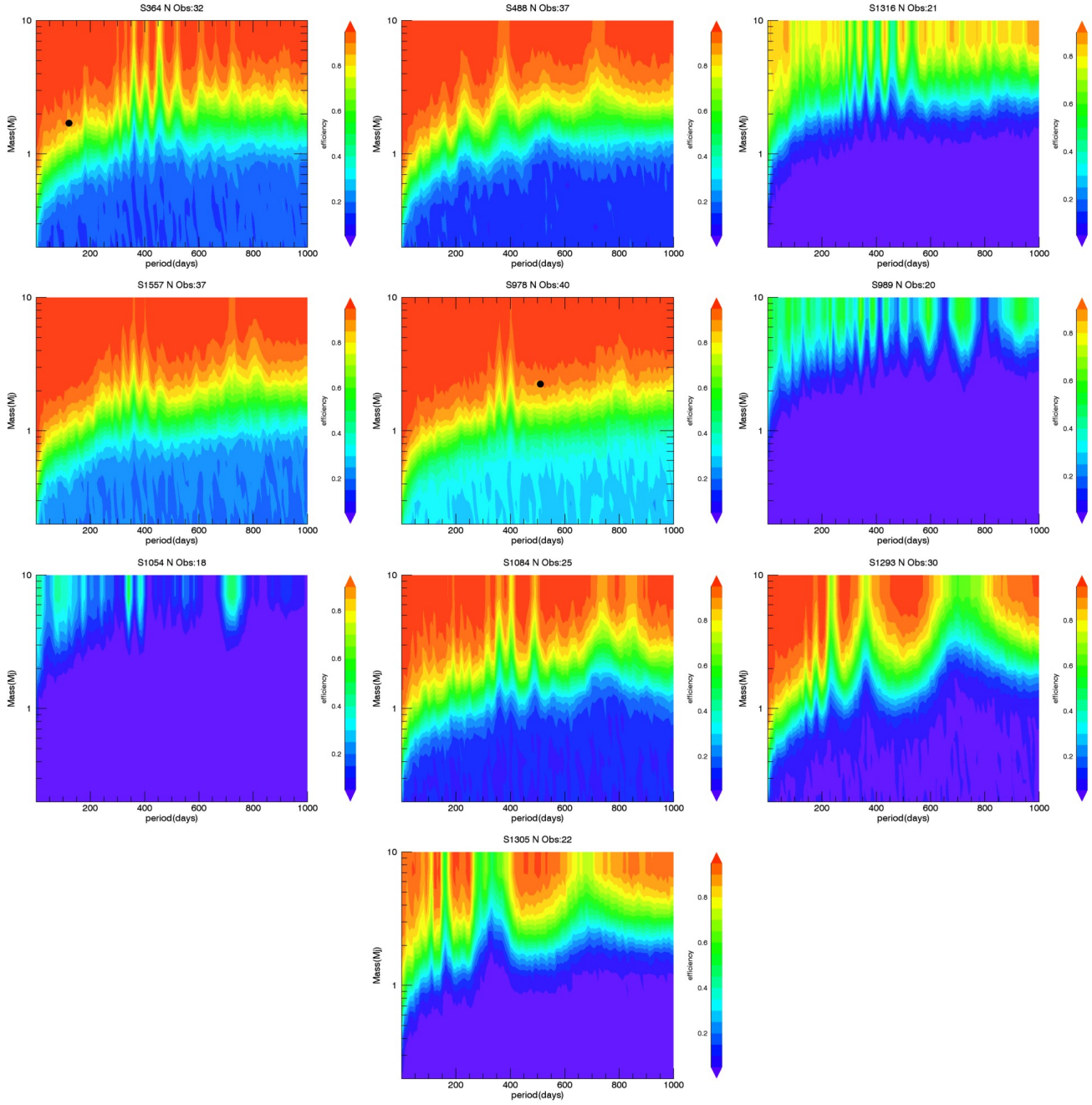

Fig. A.2. Contours of the planet detection efficiency for the evolved stars in the domains of 1–1000 days for planet period and 0.2–10 M_J for planet mass. A 0.01 FAP level has been used as detection planet threshold in the periodogram analysis. A filled circle indicates the planet position.

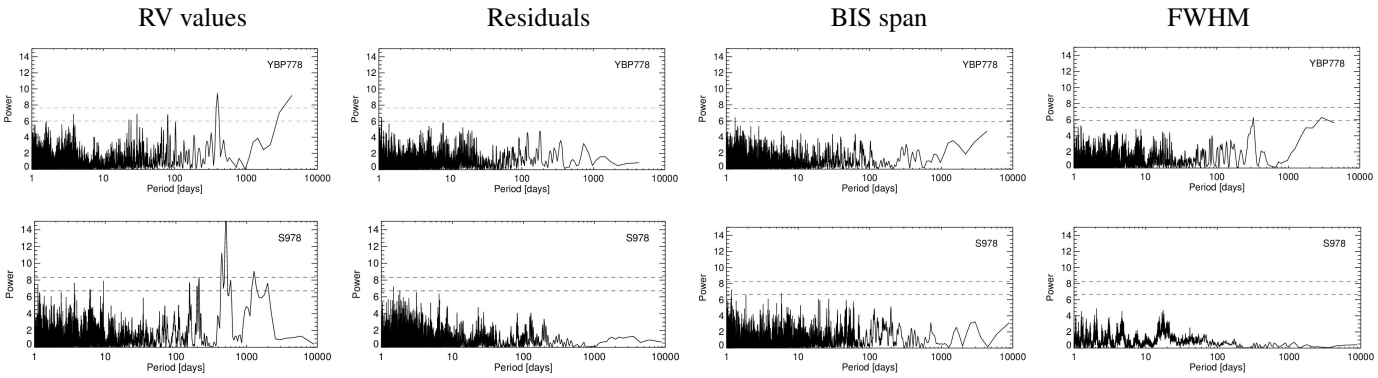

Fig. A.3. *Top*: Lomb-Scargle periodogram of the RV measurements, residuals, bisector span, and FWHM for YBP778. *Bottom*: same plots for S978. The dashed lines correspond to 5% and 1% FAPs, calculated according to Horne & Baliunas (1986) and white noise simulations.

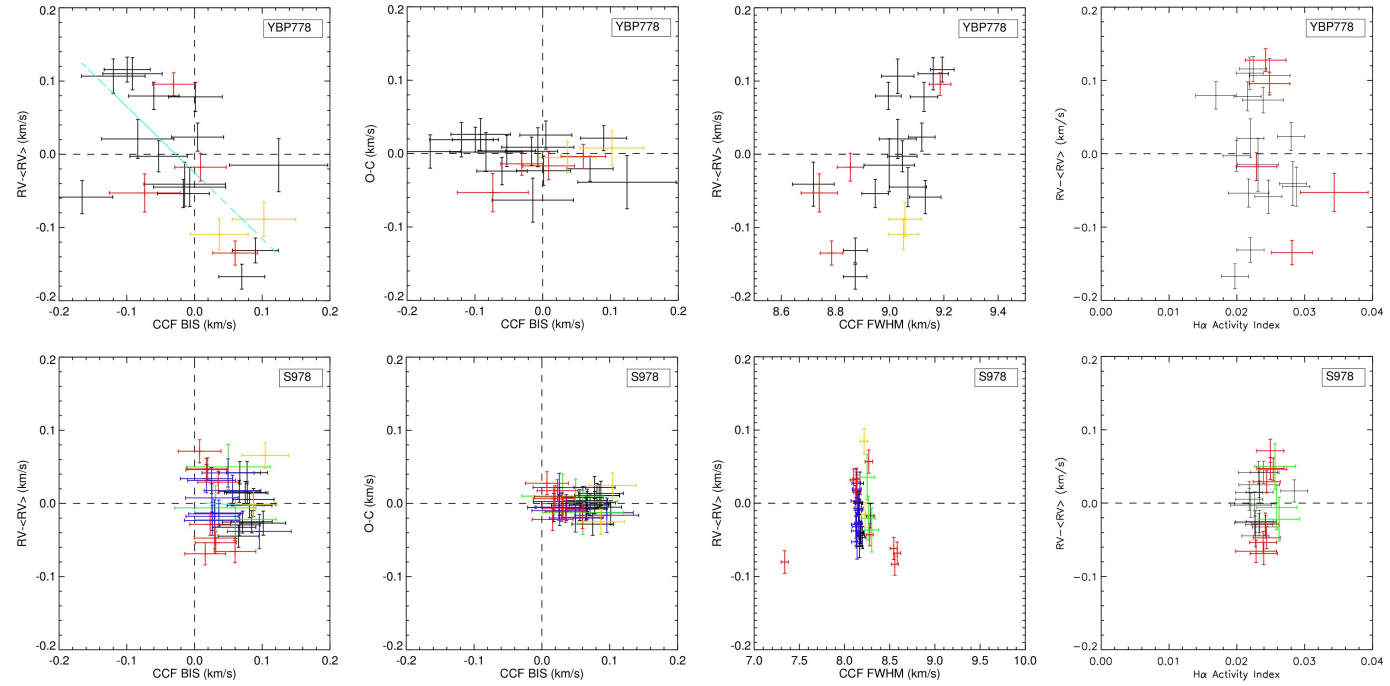

Fig. A.4. *Top*: RV measurements versus bisector span, residuals versus bisector span, RV measurements versus CCF FWHM, and RV measurements versus Hα activity indicator for YBP778. The Hα activity indicator is computed as the area below the core of Hα line with respect to the continuum. CCF FWHM values are calculated by subtracting in quadrature the respective instrumental FWHM. The same symbols as in Fig. 4. *Bottom*: same plots for S978.